Korean J. Chem. Eng., 39(10), 2817-2825 (2022)
DOI: 10.1007/s11814-022-1170-8

pISSN: 0256-1115
eISSN: 1975-7220

Optimization of Pt loading on the counter electrode for efficient and bifacial dye-sensitized solar cells with polymer gel electrolyte

Joo-Won Seo[‡], Sung-Mok Jung[‡], Yun-Jae Kim, and Jae-Yup Kim[†]

Department of Chemical Engineering, Dankook University, Yongin 16890, Korea
(*Received 11 January 2022 • Revised 20 April 2022 • Accepted 10 May 2022*)

Abstract−We examined the optimized conditions for preparing Pt/FTO glass counter electrodes (CEs) for the fabrication of highly efficient, bifacial, and quasi-solid-state dye-sensitized solar cells (QSS-DSSCs). The Pt/FTO glass CEs were prepared via thermal decomposition, and the molar concentration of the employed Pt precursor solution was controlled in the range of 5-40 mM. Impedance analysis and Tafel polarization curves revealed that electrocatalytic activity was optimized at 20 mM, whereas specular transmittance gradually decreased with increasing concentration of the precursor solution. When the CEs were applied to bifacial QSS-DSSCs employing a polymer gel electrolyte, the power conversion efficiency (PCE) was maximized at 20 mM under front illumination because the condition resulted in the highest electrocatalytic activity. Meanwhile, PCE under back illumination was optimized at 10 mM because of the larger incident light loss by the CEs at higher concentrations. Because the influence of the inferior performance under back illumination was more dominant in bifacial operations, the average PCE under front and back illumination was optimized at 10 mM.

Keywords: Bifacial Dye-sensitized Solar Cells, Pt Counter Electrode, Polymer Gel Electrolyte, Quasi-solid-state, Electrocatalytic Activity

INTRODUCTION

Photovoltaic power generation has attracted significant attention as a solution to growing energy demands caused by increasing population and industrial growth [1]. In particular, next-generation solar cells, such as organic [2-4], dye-sensitized [5-7], quantum dot [8-11], and perovskite solar cells [12-14], have attracted great interest as alternatives to conventional crystalline Si solar cells owing to their low materials cost, easy fabrication process, light weight, and flexibility [15]. Among them, dye-sensitized solar cells (DSSCs) offer unique attractive features compared to other next-generation solar cells, including semitransparent and colorful properties, low production cost, and reliability [16,17]. Another well-known advantage is their excellent performance under ambient light conditions, such as indoor operation [18,19]. Because of these features, DSSCs are often considered for window applications in building-integrated photovoltaics, which harvest the ambient light from lamps inside the building as well as incident sunlight [20-22]. Approximately 50% more electric power can be produced via this bifacial operation of photovoltaics [23,24]. For the implementation of highly efficient bifacial DSSCs, the incident light loss under back illumination should be reduced, as shown in Fig. 1(a). Therefore, the light transmittance of the counter electrode (CE) must be considered.

Platinum (Pt) is typically utilized as a CE material in DSSCs because of its superior electrocatalytic activity when employed with the commonly used iodide/triiodide redox couple (I^-/I_3^-) [25,26]. For application in bifacial DSSCs, Pt CEs are generally coated on fluorine-doped tin oxide (FTO) glasses by sputtering or thermal decomposition to yield semitransparent Pt/FTO glass CEs [24,27]. To obtain a sufficiently high electrocatalytic activity of Pt/FTO glass CEs, more than a certain amount of Pt loading is necessary. However, high Pt loading generally leads to low light transmittance of the CEs, which is disadvantageous for back-illumination operations. Owing to this trade-off relationship, Pt loading on FTO glass should be optimized for highly efficient bifacial DSSCs. However, studies on the correlation between the Pt loading on CEs and the photovoltaic performances of DSSCs in bifacial operations are scarce.

Another important issue in the commercialization of DSSCs is their inferior long-term stability, which mainly results from the evaporation and leakage of their liquid electrolyte. Therefore, many studies have focused on replacing liquid electrolytes with solid-state or quasi-solid-state electrolytes, such as solid hole conductors and polymer gel electrolytes [28-32]. However, in terms of performance, such as ionic conductivity, these electrolytes generally perform differently from conventional liquid electrolytes. Thus, the optimized conditions for the fabrication of highly efficient CEs may also be different.

In this study, we examined the optimized conditions for preparing Pt/FTO glass CEs for the fabrication of highly efficient, bifacial, and quasi-solid-state DSSCs (QSS-DSSCs). Pt/FTO glass CEs were prepared via simple thermal decomposition process, and the molar concentration of the Pt precursor solution was controlled in the range of 5-40 mM. The optical properties and electrocatalytic activities of the Pt/FTO glass CEs were examined with varying concentration of the Pt precursor solution. In addition, the effect of the optical and electrocatalytic properties of Pt/FTO glass CEs on the photovoltaic performance of QSS-DSSCs with a polymer gel elec-

[†]To whom correspondence should be addressed.
E-mail: jykim@dankook.ac.kr
[‡]These authors contributed equally to this work.

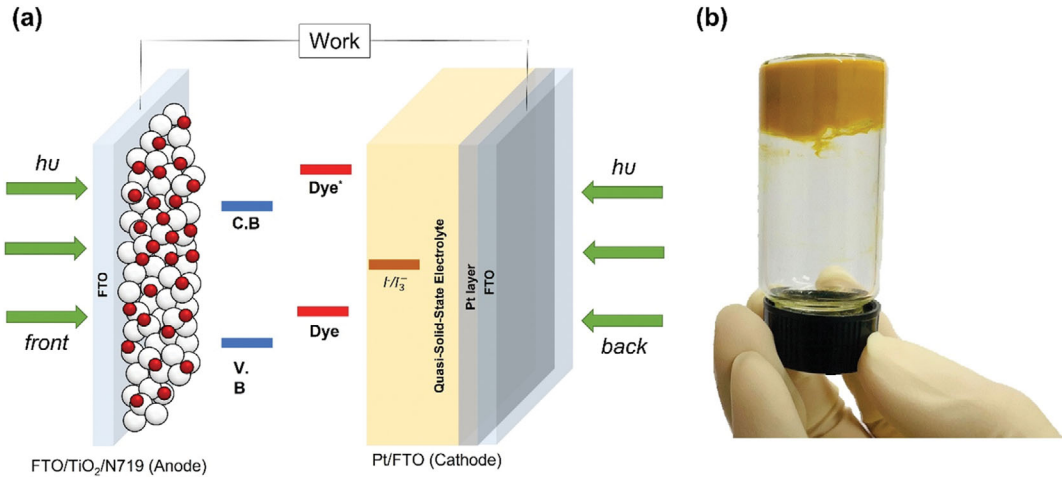

Fig. 1. (a) Schematic illustration of the bifacial DSSCs with polymer gel electrolyte under front and back illumination and (b) digital photograph of polymer gel electrolyte.

trolyte was examined to determine the optimal conditions for achieving a high power conversion efficiency (PCE) of QSS-DSSCs in bifacial operations.

EXPERIMENTAL

1. Preparation of Poly (Ethylene Oxide) (PEO)-Based Gel Electrolyte

The PEO-based gel electrolyte was prepared as described previously [33]. Briefly, 40 mg of TiO_2 nanopowder (99.5%, Aldrich) was dispersed in 50 mL of acetonitrile (99.9%, Aldrich). Then, 100 mg of LiI (99.9%, Aldrich) and 20 mg of I_2 (99.8%, Aldrich) were dissolved in solution, and 260 mg of PEO powder (Aldrich, MW= 2×10^6) was added gradually and stirred for 24 h. The prepared solution was then evaporated to obtain a viscous gel electrolyte, as shown in Fig. 1(b).

2. Fabrication of Dye-sensitized Working Electrodes

Fluorine-doped tin oxide (FTO (TEC-8, Pilkington, 8 Ω/sq) glasses were cleaned in acetone (99.5%, Daejung) and ethyl alcohol (94.5%, Daejung) under sonication for 15 min each and dried using a stream of air. The FTO glasses were treated with UV/O_3 (UV/Ozone cleaner, Yuil Ultraviolet System) for 15 min. Onto the surface of cleaned FTO glasses, titanium diisopropoxide-bis(acetylacetonate) (7.5 wt%, Aldrich) in n-butanol (99%, Daejung) was coated by spin-casting, subsequently sintered at 450 °C for 10 min. Using doctor blade technique, a transparent TiO_2 paste (Ti-Nanoxide T/SP, Solaronix) was coated on the pretreated FTO glasses, which were then sintered in ambient air at 525 °C for 30 min. Finally, the resulting FTO/TiO_2 electrodes were immersed in an ethanolic solution of 0.5 mM N719 dye (Dyesol, Australia) for 24 h.

3. Preparation of Pt CEs and Cell Assembly

To fabricate Pt CEs, Pt precursor solutions with varying molar concentrations were prepared as follows: chloroplatinic acid hexahydrate (37.5%, Aldrich) was dissolved in isopropyl alcohol (99.9%, Daejung) at concentrations of 5-40 mM. Each Pt precursor solution was spin-coated onto the surface of the pre-cleaned FTO glass and subsequently heated under ambient air at 400 °C for 23 min. To fabricate sandwich-type cells, hot-melt film (Meltonix 1170-25, Solaronix) was attached onto the prepared Pt CEs. The polymer gel electrolyte was then cast onto dye-sensitized working electrodes covered by the Pt CEs. The assembled cells were fixed using a binder clip. The active area of the cells was ~0.30 cm^2. ImageJ software was used to determine the precise active area of the electrodes.

4. Characterization

The UV-vis absorption, transmittance, and reflectance spectra of the Pt CEs were measured using UV-vis spectroscopy (OPTIZEN 2120 UV, KLAB). The structure and morphology of the Pt CEs were characterized using a field-emission scanning electron microscope (FE-SEM, S-4700, Hitachi). Elemental mapping of the Pt CEs was performed using an SEM (CX-200, COXEM) with an energy dispersive X-ray spectroscopy (EDX) detector. The surface compositions and electronic states were examined using X-ray photoelectron spectroscopy (XPS, K-alpha+, Thermo Fisher). Sheet resistance was evaluated using a four-point probe (CMT-100S, AIT). Current density-voltage (*J-V*) curves were recorded using a solar simulator (PEC-L01, Peccell) with an AM1.5G filter under 1 sunlight intensity (100 mW/cm^2). To avoid overestimating the performance of DSSCs, a black aperture mask was used for each cell during *J-V* measurements. Incident photon-to-current conversion efficiency (IPCE) spectra were obtained using a xenon lamp (Oriel 300 W) with a monochromator (TracQBasic 6.5, Oriel) and a NIST-certified Si-based diode. Symmetric dummy cells with an active area of ~1.0 cm^2 were prepared by assembling two identical Pt CEs to characterize electrocatalytic activities. The Tafel polarization curves and electrochemical impedance spectra were achieved for dummy cells using a potentiostat (Multi Autolab M204, Metrohm) equipped with a frequency-response detector. For electrochemical impedance spectroscopy (EIS) measurements, a sinusoidal perturbation of ±10 mV was applied with a frequency range of 10^{-1} to 10^5 Hz.

RESULTS AND DISCUSSION

Fig. 2(a) shows digital photographs of the Pt/FTO glass CEs prepared using different molar concentrations of the Pt precursor solu-

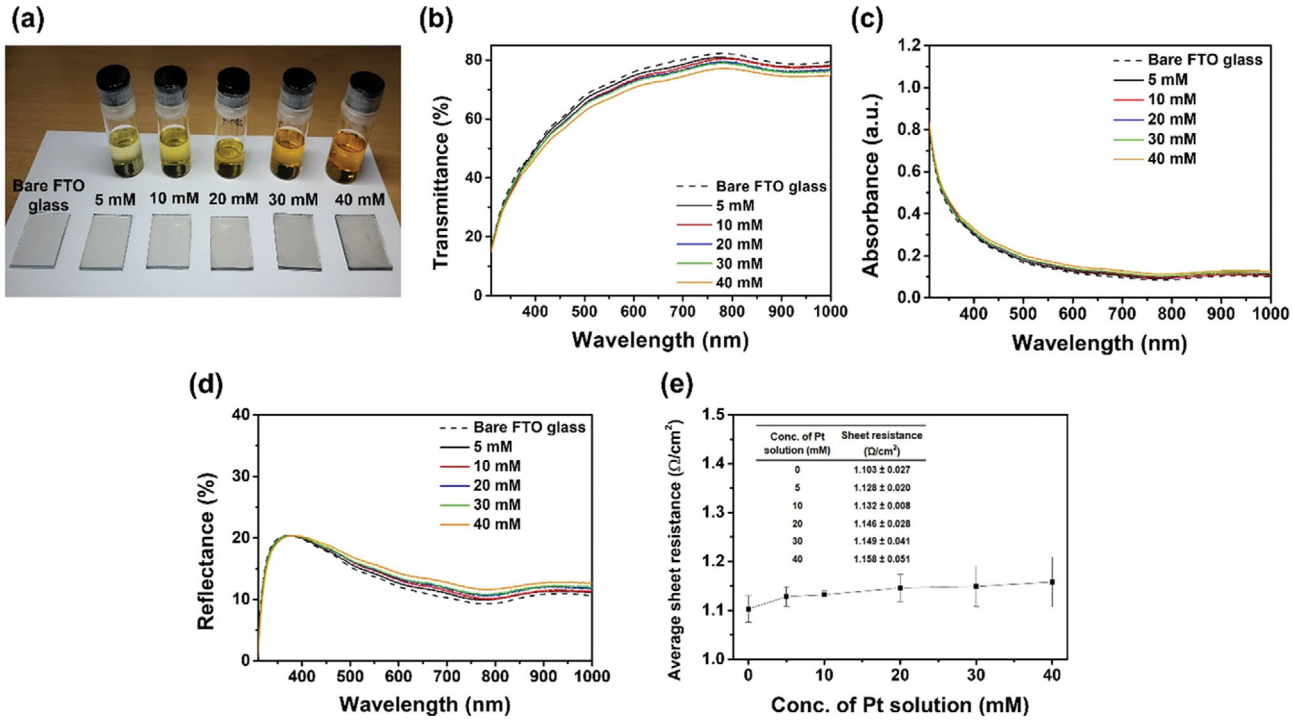

Fig. 2. (a) Digital photographs, (b) specular transmittance spectra, (c) absorbance spectra, (d) reflectance spectra, and (e) sheet resistance of Pt/FTO glass CEs depending on the molar concentration of Pt precursor solution.

tion. Evidently, the color of the precursor solution changed from pale yellow to dark yellow as the concentration increased. Moreover, the transmittance of the prepared Pt/FTO glass CEs gradually decreased with increasing concentration of the Pt precursor solution. In particular, the Pt/FTO glass CEs exhibited a non-uniform color distribution at concentrations exceeding 30 mM. Fig. 2(b)-(d) shows the UV-vis spectra of the Pt/FTO glass CEs. As shown in Fig. 2(b), although specular transmittance gradually decreased with increasing concentration, all samples exhibited semi-transparency in the whole visible range. To reduce the efficiency loss under back-illumination operation, the transmittance at 535 nm corresponding to the absorption peak position of N-719 dye is important for the CEs. The transmittances at this wavelength of bare FTO glass, 5 mM, 10 mM, 20 mM, 30 mM, and 40 mM are 70.98%, 69.78%, 68.51%, 68.02%, 67.80%, and 65.84%, respectively. In addition, as shown in Fig. 2(c) and (d), the absorbances at 535 nm are 0.149, 0.156, 0.164, 0.167, 0.169, and 0.182, and the reflectances at 535 nm are 14.13%, 14.62%, 15.09%, 15.28%, 15.30%, and 15.96% for 5 mM, 10 mM, 20 mM, 30 mM, and 40 mM sample, respectively. These results imply that although both the absorbance and reflectance gradually increase as the concentration is raised, all samples exhibit sufficiently high transparency for application in bifa-

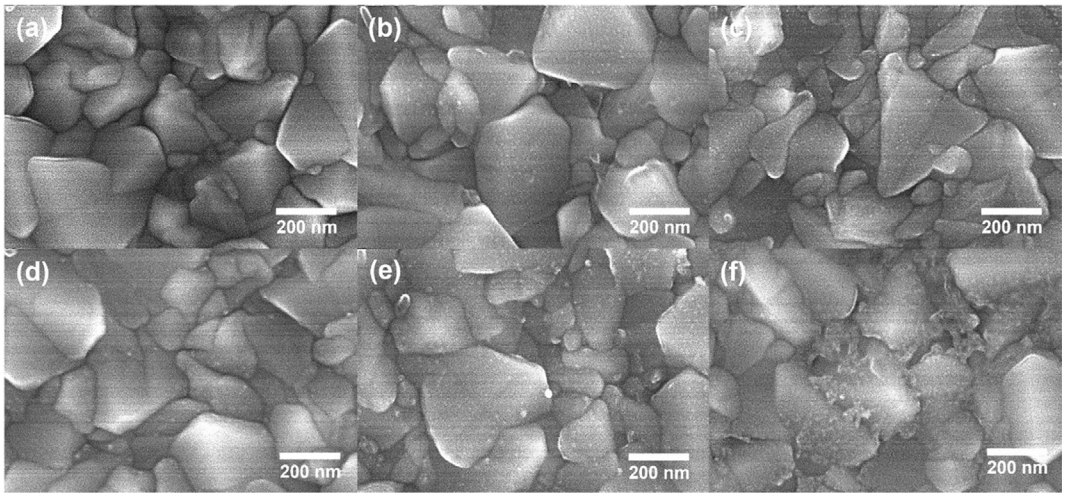

Fig. 3. Surface SEM images of Pt/FTO glass CEs depending on the molar concentration of Pt precursor solution. (a) 0 mM, (b) 5 mM, (c) 10 mM, (d) 20 mM, (e) 30 mM, and (f) 40 mM.

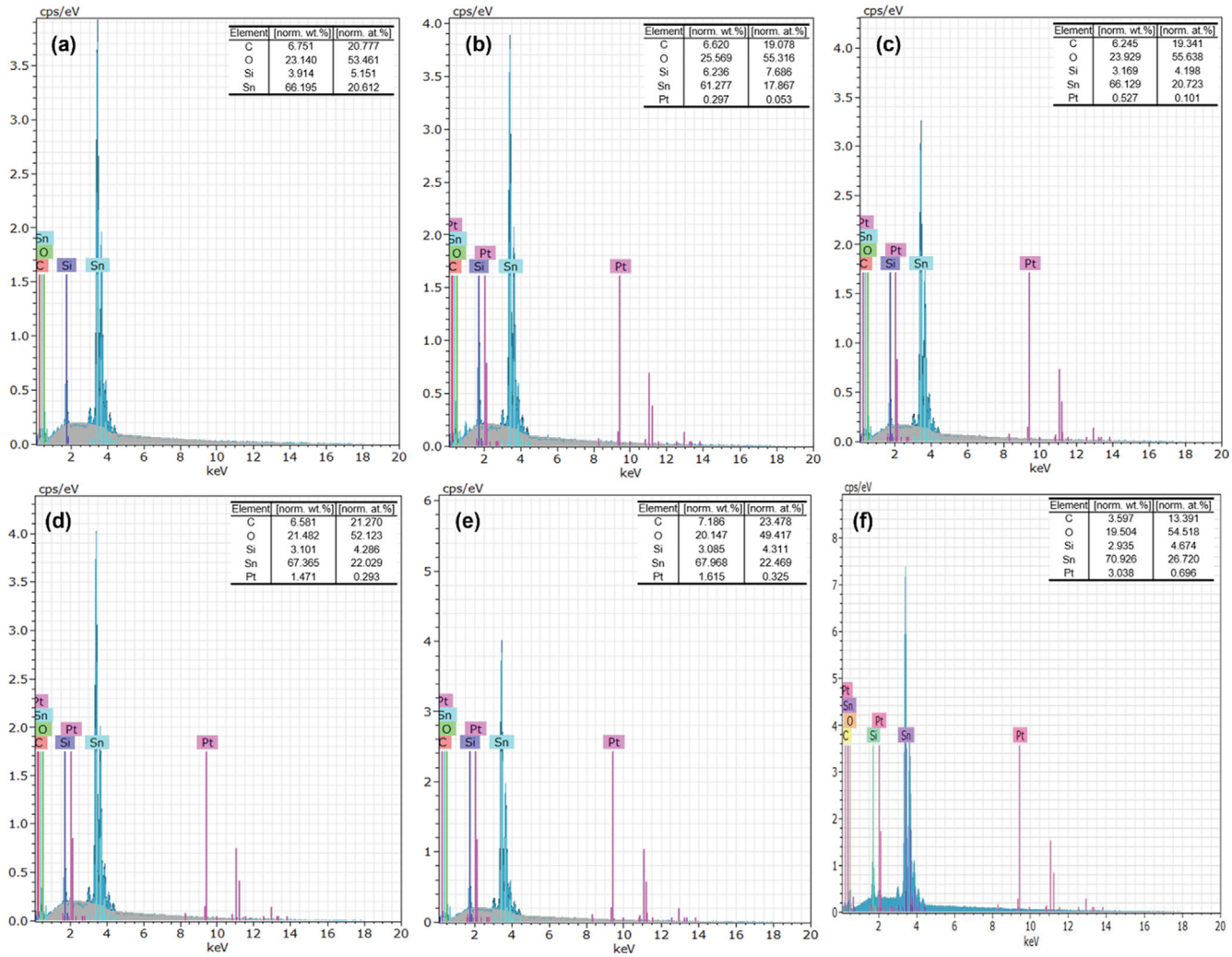

Fig. 4. EDX results of Pt/FTO glass CEs depending on the molar concentration of Pt precursor solution. (a) 0 mM, (b) 5 mM, (c) 10 mM, (d) 20 mM, (e) 30 mM, and (f) 40 mM.

cial DSSCs.

Fig. 2(e) shows the sheet resistance of the Pt/FTO glass CE. Sheet resistance gradually increased with increasing concentration of the Pt precursor solution. As a result, the sheet resistance of the bare FTO glass and 40 mM sample was 1.103 and 1.158 Ω/cm^2, respectively. Therefore, the electrical conductivity of the coated Pt layer is lower than that of bare FTO. The difference in conductivity may be attributed to the remaining contaminants and the chemical states of the coated Pt, which will be discussed later.

The surface morphology of the Pt/FTO glass CEs was examined by FE-SEM as shown in Fig. 3. In contrast to the bare FTO glass (Fig. 3(a)), the coated Pt particles are shown on the Pt/FTO glasses (Fig. 3(b)-(f)). In addition, it is distinct that the coated Pt particles became larger with increasing concentration of the Pt precursor solution. However, it seems that these coated Pt did not form a film-like structure but a discontinuous island-like structure. In the cross-sectional FE-SEM images of the Pt/FTO glass CEs (Fig. S1), it is difficult to find significant differences between the samples, since the coated Pt particles are smaller than the roughness of FTO glass.

The increase in Pt loading on FTO glass with increasing concentration of the precursor solution was confirmed by an FE-SEM instrument equipped with EDX. Fig. 4 shows the EDX spectra obtained from the top view of the Pt/FTO glass CEs. Elements in the FTO glass, coated Pt catalysts, and carbon contaminants were detected. According to the EDX results, the Pt contents coated on the FTO glass increased by approximately 1.9, 5.5, 6.1, 13.1 times for the 10, 20, 30, and 40 mM samples, respectively, compared to that of the 5 mM sample. The amount of Pt loading on the FTO glass gradually increased with the increasing concentration of the Pt precursor solution. In addition, it is conjectured that the carbon contaminants result from the incomplete combustion of organic species, such as isopropyl alcohol.

The surface chemistry of the Pt/FTO glass CEs was investigated by XPS measurement. Fig. S2 shows the spectra of Pt/FTO glass CEs over a wide scan range, which exhibits the presence of Pt, C, and Cl for all samples. The C and Cl contaminants may be attributed to the incomplete combustion of organic species and Pt precursor (chloroplatinic acid hexahydrate), respectively. In addition, as listed in Table S1, the Pt content gradually increased with increasing con-

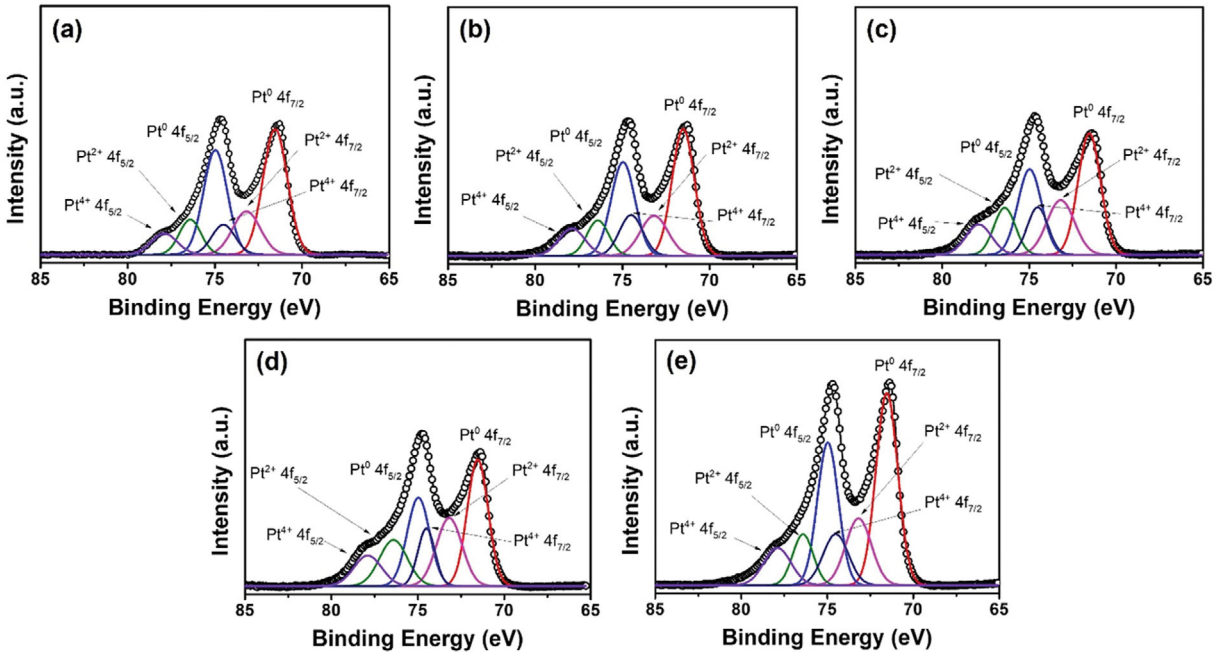

Fig. 5. High-resolution XPS spectra of Pt 4f for Pt/FTO glass CEs depending on the molar concentration of Pt solution. (a) 5 mM, (b) 10 mM, (c) 20 mM, (d) 30 mM, (e) 40 mM.

centration, which accords well with the EDX results. In particular, to examine the surface state of the Pt, high-resolution scans of Pt 4f were analyzed as shown in Fig. 5. These spectra can be deconvoluted into three doublets with spin-orbit coupling of about 3.3 eV, which can be assigned to metallic Pt, Pt^{2+}, and Pt^{4+}, respectively. The binding energy (BE) values for these Pt 4f peaks were nearly constant regardless of the concentration of the precursor solution concentration conditions. The Pt $4f_{7/2}$ peak at 71.6 eV and Pt $4f_{5/2}$ peak at 74.9 eV are attributed to the metallic Pt [34,35], while the Pt $4f_{7/2}$ peak at 73.1 eV and Pt $4f_{5/2}$ peak at 76.4 eV are assigned to the Pt^{2+} in PtO [36,37]. In addition, the Pt $4f_{7/2}$ peak at 74.5 eV and Pt $4f_{5/2}$ peak at 77.8 eV can be assigned to the Pt^{4+} in $PtCl_4$ [38]. Comparison of the peak areas revealed that the coated Pt content mainly existed in the metallic state, and partly existed in the form of oxide or remained in the initial chemical state of precursor (chloroplatinic acid hexahydrate). These results indicate that the increase in sheet resistance of the Pt/FTO glass compared to the bare FTO glass was attributed to the Pt content in the nonmetallic state as well as the C and Cl contaminants.

Symmetric dummy cells with Pt/FTO glass CEs were fabricated to compare quantitatively the electrocatalytic activity (Fig. 6(a)). Fig. 6(b) shows the impedance data achieved from the symmetric dummy cells, depending on the concentration of the Pt precursor solution. Based on these spectra, impedance parameters were evaluated using the equivalent circuit model shown in the inset of Fig. 6(b) and the ZView software. The equivalent circuit model is composed of the series resistance (R_s), finite Warburg impedance (W_s) related with the diffusion of redox couples in the electrolyte, and impedance at the interface between the electrolyte and Pt/FTO glass CEs (R_{ct} and CPE) [39-41]. Based on the charge transfer resistance (R_{ct}) between the CEs and the iodide/triiodide redox couple in the electrolyte, the electrocatalytic activity of the CEs can be qualitatively compared. In addition, from the CPE parameters, the double-layer capacitance (C_{dl}) of the CEs can be evaluated. The diffusion resistance of the electrolyte (R_{Dif}) was determined from the W_s values.

Table 1. Parameters determined by fitting the impedance spectra of symmetric dummy cells with Pt/FTO glass CEs depending on the molar concentration of Pt precursor solution

Concentration of Pt precursor solution	R_s (Ω cm^2)	R_{ct} (Ω cm^2)	C_{dl} (μF/cm^2)	R_{Dif} (Ω cm^2)
5 mM	3.953	1.677	15.702	1.634
10 mM	3.558	0.832	26.898	1.642
20 mM	3.875	0.321	33.818	1.428
30 mM	3.733	0.322	29.574	1.310
40 mM	2.965	0.401	55.398	1.461

The fitted impedance parameters for each CE are listed in Table 1. The R_s and R_{Dif} values did not differ significantly with respect to the different concentrations of the Pt precursor solution. The R_s values were slightly varied; however, this variation can be considered as experimental error when compared to the previous studies [42,43]. Since the same substrate (FTO glass) and electrolyte were employed for each device, it is reasonable to assume that R_s and R_{Dif} values cannot be different for each condition. Therefore, we only focused on the R_{ct} and C_{dl}, which are strongly related to the electrocatalytic properties of the electrodes. As listed in Table 1, the R_{ct} considerably decreased with the increase in concentration from 5 mM to 20 mM. The R_{ct} did not change significantly at concentration higher than 20 mM, implying that the electrocatalytic activity of the iodide/triiodide redox couple was optimized at 20 mM. In addition, the C_{dl} value increased at higher concentration conditions, meaning that the accessible surface area was en-

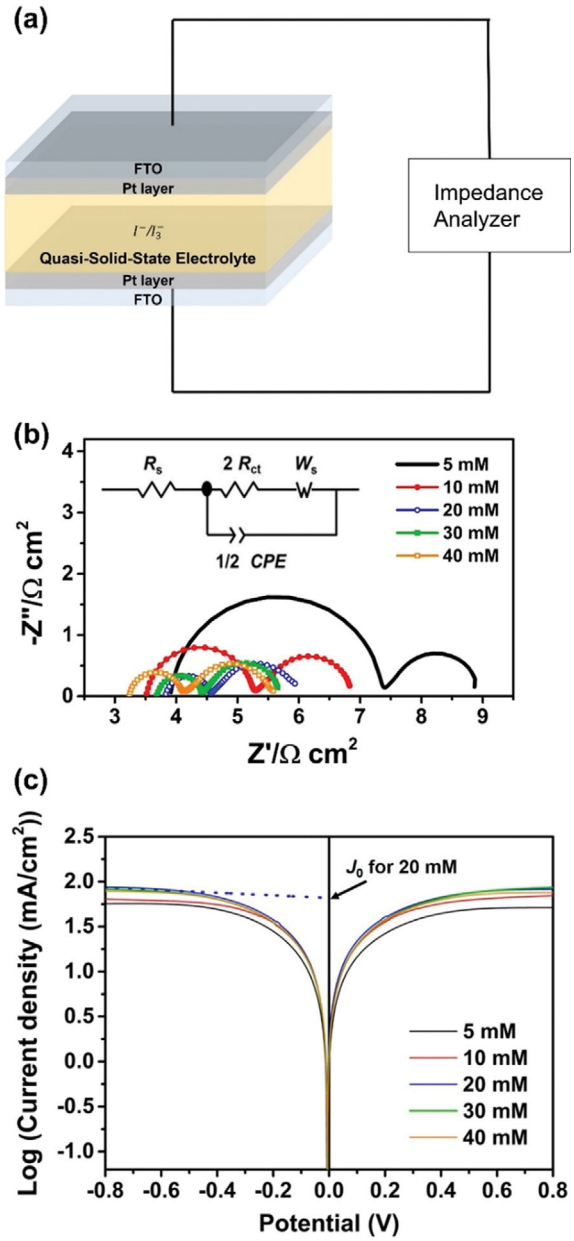

Fig. 6. (a) Schematic illustration of the symmetric dummy cell for the impedance and Tafel analyses. (b) Impedance spectra (inset: equivalent circuit model) and (c) Tafel polarization curves of symmetric dummy cells with Pt/FTO glass CEs depending on the concentration of Pt precursor solution.

hanced by increased Pt loading.

The relative electrocatalytic activity for each CE was cross-checked using Tafel polarization curves, as presented in Fig. 6(c). Exchange current density (J_0) was calculated from the intersection of the linear parts in the limiting diffusion zone [44,45]. The J_0 values for the 5, 10, 20, 30, and 40 mM samples were 1.719, 1.726, 1.819, 1.804, and 1.783 mA/cm^2, respectively. In agreement with the impedance results, the 20 mM sample exhibited the highest J_0, that is, the highest electrocatalytic activity. According to the impedance and Tafel polarization curve results, the concentration of the Pt precursor solution should be at least 20 mM to achieve the optimal

Table 2. Summary of *J-V* characteristics and integrated J_{SC} calculated from IPCE spectra for QSS-DSSCs obtained under front illumination depending on the molar concentration of Pt precursor solution

Concentration of Pt precursor solution	J_{SC} (mA/cm^2)	J_{SC} (IPCE) (mA/cm^2)	V_{OC} (mV)	FF	η (%)
5 mM	12.11	11.86	574	0.63	4.38
10 mM	13.06	12.26	589	0.66	5.08
20 mM	13.29	12.58	593	0.66	5.23
30 mM	13.31	12.21	588	0.65	5.05
40 mM	12.36	11.63	600	0.67	4.93

Table 3. Summary of *J-V* characteristics and integrated J_{SC} calculated from IPCE spectra for QSS-DSSCs obtained under back illumination depending on the molar concentration of Pt precursor solution

Concentration of Pt precursor solution	J_{SC} (mA/cm^2)	J_{SC} (IPCE) (mA/cm^2)	V_{OC} (mV)	FF	η (%)
5 mM	8.52	7.88	578	0.66	3.24
10 mM	9.23	8.94	545	0.70	3.51
20 mM	8.75	8.52	540	0.69	3.25
30 mM	8.33	7.78	550	0.67	3.08
40 mM	7.50	7.01	557	0.71	2.95

electrocatalytic activity. This optimal electrocatalytic activity originated from the trade-off relation between the increase in sheet resistance of the substrate and the enhanced Pt loading with increasing concentration of the Pt precursor solution, which was confirmed by EDX and XPS analyses.

After the prepared Pt/FTO glass CEs were applied in bifacial QSS-DSSCs, their photovoltaic performance was examined depending on the concentration of the Pt precursor solution. Fig. 7(a) represents the *J-V* curves of the QSS-DSSCs under front illumination with varying concentration of the Pt precursor solution. The photovoltaic parameters are listed in Table 2. Compared to that of the 5 mM sample, the photovoltaic performance of the 10 and 20 mM samples, particularly the J_{SC} and fill factor (FF), was enhanced. These results are attributed to the gradual increase in electrocatalytic activity, as discussed above. By contrast, the 40 mM sample exhibited slightly reduced J_{SC} and PCE compared to the 20 mM sample. This difference may be due to decreased sheet resistance. As a result, PCE was optimized at 20 mM, as expected from the electrocatalytic activity results above. Fig. 7(b) presents the IPCE results of QSS-DSSCs under front illumination. The IPCE spectra of all QSS-DSSCs exhibited similar shapes regardless of the concentration of the precursor solution. Based on these spectra, the integrated J_{SC} was calculated using publicly available data for AM 1.5G solar irradiation [46], as listed in Table 2. These results agree well with the J_{SC} values obtained from the *J-V* curves.

The photovoltaic performance was significantly different for the back-illumination operation, as shown in Fig. 7(c) and 7(d). Fig. 7(c) shows the *J-V* curves of QSS-DSSCs under back illumination with varying concentration of the Pt precursor solution. The photovoltaic parameters are listed in Table 3. In contrast to the front-

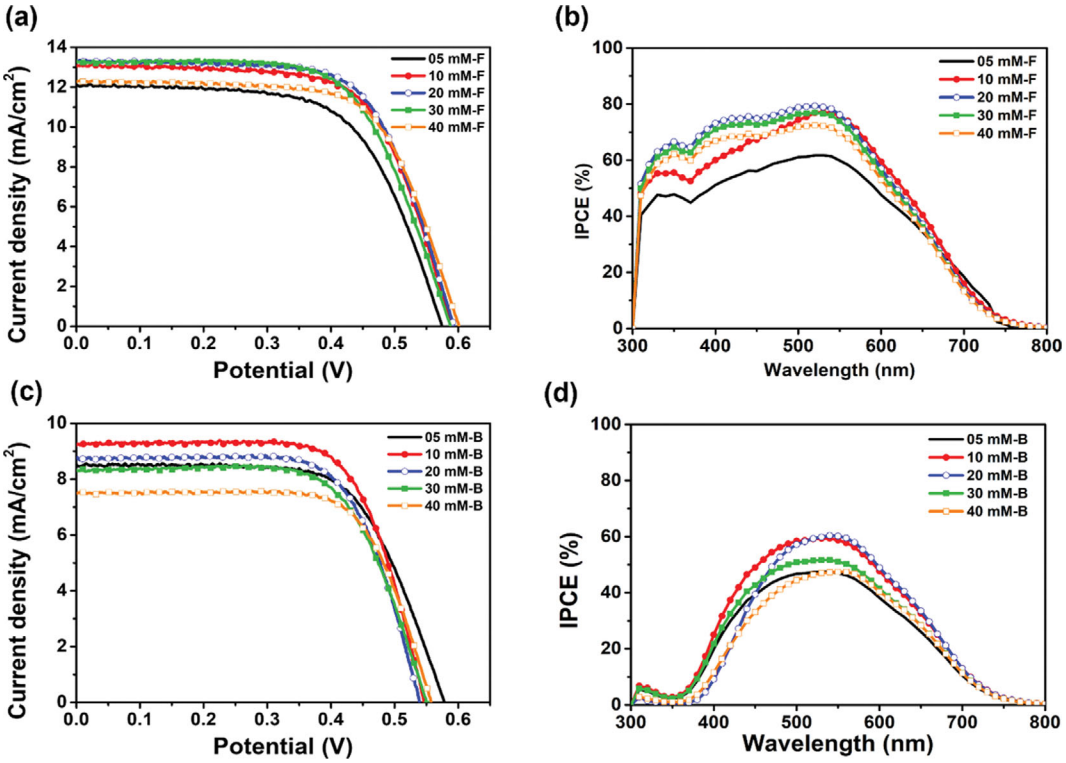

Fig. 7. *J-V* curves (a), (c) and IPCE spectra (b), (d) of QSS-DSSCs obtained under front (a), (b) and back illumination (c), (d) depending on the concentration of Pt precursor solution.

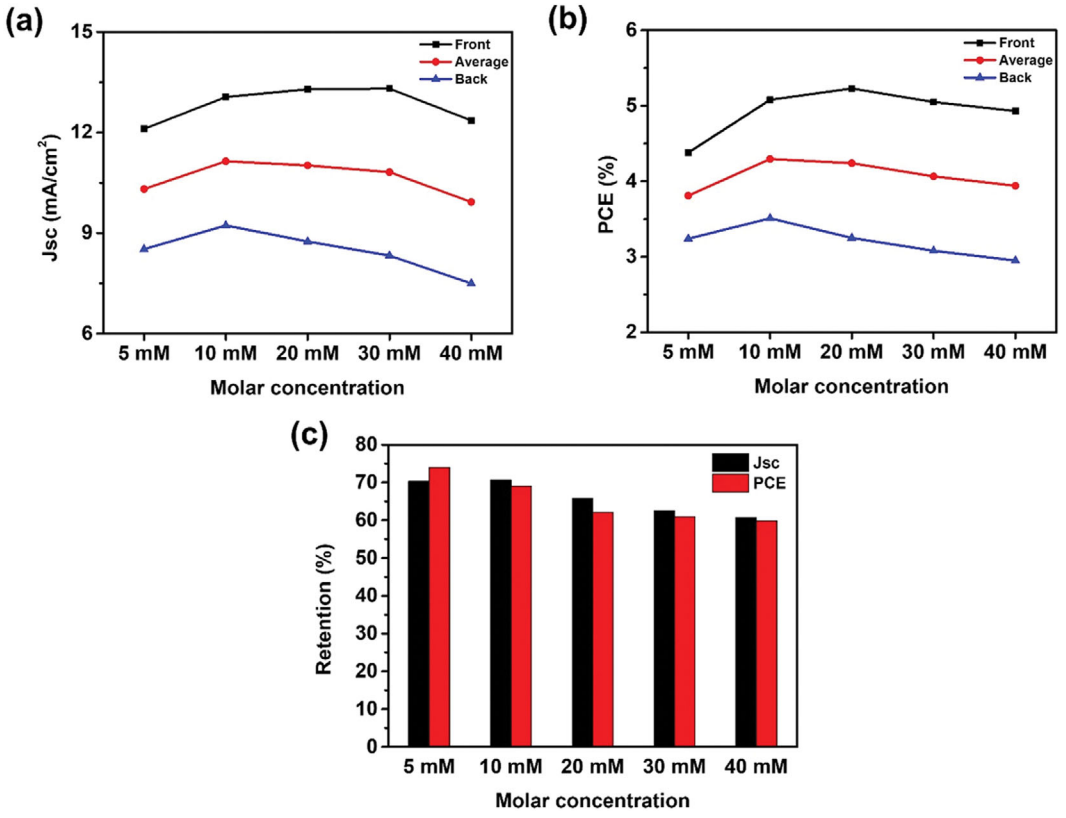

Fig. 8. Dependence of (a) J_{SC} and (b) PCE, and (c) retention rates (ratio of J_{SC} and PCE measured under front and back illumination) on the concentration of Pt precursor solution.

illumination conditions, back illumination did not result in significantly different PCE values with varying concentration of the precursor solution. Compared to that of the 5 mM sample, the FF values at higher concentration were enhanced because of increased electrocatalytic activity. Meanwhile, V_{OC} values decreased because of incident light loss by the CE and electrolyte. J_{SC} was optimized at 10 mM and gradually decreased at higher concentration. This trend is attributed to the trade-off between the superior electrocatalytic activity and increased incident light loss at high concentration. In Fig. 2(b), the transmittance of the CE decreases at high concentration, resulting in considerable incident light loss under back illumination. As a result, PCE was optimized at 10 mM.

Fig. 7(d) represents the IPCE results of the QSS-DSSCs under back illumination. The shapes of the IPCE curves are evidently different from those obtained under front illumination. This difference is due to incident light loss by the CEs and electrolyte, particularly in the short-wavelength region. The comparison of IPCE spectra obtained under front and back illumination (Fig. S3) indicates that the discrepancy is relatively small in the long-wavelength region, however, particularly significant in the short-wavelength region for all samples. For example, for the 20 mM sample, the discrepancy between IPCE values obtained under front and back illumination was smaller than 10% in the wavelength region longer than 600 nm, while it was about 10-66% in the wavelength region shorter than 600 nm. Given that the differences of absorbance and reflectance are small between the bare FTO glass and the Pt/FTO glass, and the difference of transmittance is lower than 5-6% (Fig. 2(b)-(d)), the great discrepancy in the short-wavelength region is mainly attributed to the incident light loss by the iodide/triiodide electrolyte. According to the previous study, the iodide/triiodide electrolyte exhibits strong absorption in the wavelength region shorter than 650 nm [47]. This absorption property of the iodide/triiodide electrolyte accords well with the IPCE data for the back illumination condition. The integrated J_{SC} from the IPCE results are listed in Table 3, and these results agree well with the J_{SC} achieved from the *J-V* curves.

For the efficient bifacial operation of solar cells, the PCE values under both front and back illumination are important. Fig. 8(a) and 8(b) show the dependence of J_{SC} and PCE on the concentration of the Pt precursor solution under both front and back illumination. Under front illumination, the J_{SC} and PCE were optimized at 30 and 20 mM, respectively, whereas both values were optimized at 10 mM under back illumination. As represented in Fig. 8(c), the J_{SC} and PCE retention rates are lower at 20 mM compared to those at 10 mM. These retention rates correspond to the ratios between photovoltaic performance parameters achieved under back and front illumination. Consequently, the average J_{SC} and PCE were optimized at 10 mM, which means that this concentration is the best condition for the efficient bifacial operation of QSS-DSSCs. These results indicate that in the fabrication of highly efficient and bifacial QSS-DSSCs, the electrocatalytic activity of CEs as well as the prevention of incident light loss are important. To further improve the PCE of bifacial QSS-DSSCs, more detailed studies on the development of new CEs and quasi-solid-state electrolytes that satisfy both excellent performance and high transparency requirements should be conducted.

CONCLUSIONS

Pt/FTO glass CEs were fabricated by a simple thermal decomposition with varying concentration of the Pt precursor solution. The prepared Pt/FTO glass CEs were applied to the QSS-DSSCs using a polymer gel electrolyte. The specular transmittance of the CEs gradually decreased with the increasing concentration of the Pt precursor solution. The electrocatalytic activity of the iodide/triiodide redox couple was optimized at 20 mM, as confirmed by impedance analysis and Tafel polarization curves. Under front illumination, PCE was maximized at 20 mM because the condition yielded the best electrocatalytic activity. Meanwhile, PCE was maximized at 10 mM under back illumination because of the decreased transmittance of CEs at concentration higher than the optimal. As a result, the average PCE under front illumination and back illumination was optimized at 10 mM, which is the best condition for the fabrication of highly efficient and bifacial QSS-DSSCs. The obtained results provide valuable insights into the development of highly efficient bifacial DSSCs with long-term stability.

ACKNOWLEDGEMENTS

This work was supported by the National Research Foundation of Korea (NRF) grant funded by the Korea government (MSIT) (No. 2020R1C1C1012014 and No. 2021M3I3A1085039). This work was also funded by the University Innovation Support Program for Dankook University in 2021.

SUPPORTING INFORMATION

Additional information as noted in the text. This information is available via the Internet at http://www.springer.com/chemistry/journal/11814.

REFERENCES

1. U. K. Das, K. S. Tey, M. Seyedmahmoudian, S. Mekhilef, M. Y. I. Idris, W. Van Deventer, B. Horan and A. Stojcevski, *Renew. Sust. Energ. Rev.*, **81**, 912 (2018).
2. Y. Cheng, S. Yang and C. Hsu, *Chem. Rev.*, **109**, 5868 (2009).
3. J. Yuan, Y. Zhang, L. Zhou, G. Zhang, H. Yip, T. Lau, X. Lu, C. Zhu, H. Peng and P. A. Johnson, *Joule*, **3**, 1140 (2019).
4. T. Aernouts, P. Vanlaeke, W. Geens, J. Poortmans, P. Heremans, S. Borghs, R. Mertens, R. Andriessen and L. Leenders, *Thin Solid Films*, **451**, 22 (2004).
5. B. O'regan and M. Grätzel, *Nature*, **353**, 737 (1991).
6. S. Hao, J. Wu, Y. Huang and J. Lin, *Sol. Energy*, **80**, 209 (2006).
7. L. Han, A. Islam, H. Chen, C. Malapaka, B. Chiranjeevi, S. Zhang, X. Yang and M. Yanagida, *Energy Environ. Sci.*, **5**, 6057 (2012).
8. J. Yang, J. Kim, J. H. Yu, T. Ahn, H. Lee, T. Choi, Y. Kim, J. Joo, M. J. Ko and T. Hyeon, *Phys. Chem. Chem. Phys.*, **15**, 20517 (2013).
9. W. Li, Z. Pan and X. Zhong, *J. Mater. Chem. A*, **3**, 1649 (2015).
10. J. Kim, J. Yang, J. H. Yu, W. Baek, C. Lee, H. J. Son, T. Hyeon and M. J. Ko, *ACS Nano*, **9**, 11286 (2015).
11. P. V. Kamat, *J. Phys. Chem. C*, **112**, 18737 (2008).
12. A. Mei, X. Li, L. Liu, Z. Ku, T. Liu, Y. Rong, M. Xu, M. Hu, J. Chen

and Y. Yang, *Science*, **345**, 295 (2014).
13. W. Yin, T. Shi and Y. Yan, *Appl. Phys. Lett.*, **104**, 063903 (2014).
14. M. Jošt, E. Köhnen, A. B. Morales-Vilches, B. Lipovšek, K. Jäger, B. Macco, A. Al-Ashouri, J. Krč, L. Korte and B. Rech, *Energy Environ. Sci.*, **11**, 3511 (2018).
15. D. Kumar and K. Wong, *Mater. Today Energy*, **5**, 243 (2017).
16. G. Y. Margulis, M. G. Christoforo, D. Lam, Z. M. Beiley, A. R. Bowring, C. D. Bailie, A. Salleo and M. D. McGehee, *Adv. Energy Mater.*, **3**, 1657 (2013).
17. H. Otaka, M. Kira, K. Yano, S. Ito, H. Mitekura, T. Kawata and F. Matsui, *J. Photochem. Photobiol. A*, **164**, 67 (2004).
18. K. Kawata, K. Tamaki and M. Kawaraya, *JPST*, **28**, 415 (2015).
19. W. Naim, V. Novelli, I. Nikolinakos, N. Barbero, I. Dzeba, F. Grifoni, Y. Ren, T. Alnasser, A. Velardo and R. Borrelli, *JACS Au.*, **1**, 409 (2021).
20. D. Hwang, J. E. Nam, H. J. Jo and S. Sung, *J. Power Sources*, **361**, 87 (2017).
21. Q. Tai, B. Chen, F. Guo, S. Xu, H. Hu, B. Sebo and X. Zhao, *ACS Nano.*, **5**, 3795 (2011).
22. S. Xu, Y. Luo, G. Liu, G. Qiao, W. Zhong, Z. Xiao, Y. Luo and H. Ou, *Electrochim. Acta*, **156**, 20 (2015).
23. A. Hübner, A. G. Aberle and R. Hezel, *Appl. Phys. Lett.*, **70**, 1008 (1997).
24. S. Ito, S. M. Zakeeruddin, P. Comte, P. Liska, D. Kuang and M. Gratzel, *Nat. Photonics*, **2**, 693 (2008).
25. J. Wu, Z. Tang, Y. Huang, M. Huang, H. Yu and J. Lin, *J. Power Sources*, **257**, 84 (2014).
26. M. Y. Song, K. N. Chaudhari, J. Park, D. Yang, J. H. Kim, M. Kim, K. Lim, J. Ko and J. Yu, *Appl. Energy*, **100**, 132 (2012).
27. X. Fang, T. Ma, G. Guan, M. Akiyama, T. Kida and E. Abe, *J. Electroanal. Chem.*, **570**, 257 (2004).
28. W. Kubo, K. Murakoshi, T. Kitamura, S. Yoshida, M. Haruki, K. Hanabusa, H. Shirai, Y. Wada and S. Yanagida, *J. Phys. Chem. B*, **105**, 12809 (2001).
29. Z. Lan, J. Wu, J. Lin, M. Huang, S. Yin and T. Sato, *Electrochim. Acta*, **52**, 6673 (2007).
30. E. Palomares, J. N. Clifford, S. A. Haque, T. Lutz and J. R. Durrant, *J. Am. Chem. Soc.*, **125**, 475 (2003).
31. J. Xia, N. Masaki, M. Lira-Cantu, Y. Kim, K. Jiang and S. Yanagida, *J. Am. Chem. Soc.*, **130**, 1258 (2008).
32. A. Hagfeldt, G. Boschloo, L. Sun, L. Kloo and H. Pettersson, *Chem. Rev.*, **110**, 6595 (2010).
33. T. Stergiopoulos, I. M. Arabatzis, G. Katsaros and P. Falaras, *Nano Lett.*, **2**, 1259 (2002).
34. Y. Devrim and E. D. Arıca, *Int. J. Hydrogen Energy*, **44**, 18951 (2019).
35. X. Yang, J. Zheng, M. Zhen, X. Meng, F. Jiang, T. Wang, C. Shu, L. Jiang and C. Wang, *Appl. Catal. B: Environ.*, **121**, 57 (2012).
36. O. Rosseler, C. Ulhaq-Bouillet, A. Bonnefont, S. Pronkin, E. Savinova, A. Louvet, V. Keller and N. Keller, *Appl. Catal. B: Environ.*, **166**, 381 (2015).
37. X. Xue, T. Lu, C. Liu, W. Xu, Y. Su, Y. Lv and W. Xing, *Electrochim. Acta*, **50**, 3470 (2005).
38. I. G. Casella and E. Desimoni, *Electroanalysis*, **8**, 447 (1996).
39. P. N. Kumar, A. Kolay, S. K. Kumar, P. Patra, A. Aphale, A. K. Srivastava and M. Deepa, *ACS Appl. Mater. Interfaces*, **8**, 27688 (2016).
40. J. D. Roy-Mayhew, D. J. Bozym, C. Punckt and I. A. Aksay, *ACS Nano*, **4**, 6203 (2010).
41. J. Kim, K. J. Lee, S. H. Kang, J. Shin and Y. Sung, *J. Phys. Chem. C*, **115**, 19979 (2011).
42. H. Jaafar, M. F. Ain and Z. A. Ahmad, *Opt. Quant. Electron.*, **52**, 221 (2020).
43. T.-Y. Hsieh, T.-C. Wei, P. Zhai, S.-P. Feng, M. Ikegami and T. Miyasaka, *J. Power Sources*, **283**, 351 (2015).
44. M. Wu, X. Lin, Y. Wang, L. Wang, W. Guo, D. Qi, X. Peng, A. Hagfeldt, M. Grätzel and T. Ma, *J. Am. Chem. Soc.*, **134**, 3419 (2012).
45. Y.-C. Wang, D.-Y. Wang, Y.-T. Jiang, H.-A. Chen, C.-C. Chen, K.-C. Ho, H.-L. Chou and C.-W. Chen, *Angew. Chem. Int. Ed.*, **52**, 6694 (2013).
46. *Reference Solar Spectral Irradiance: Air Mass 1.5*; American Society for Testing and Materials: West Conshohocken, PA, http://rredc.nrel.gov/solar/spectra/am1.5 (accessed November 23rd 2021).
47. M. Wang, N. Chamberland, L. Breau, J.-E. Moser, R. Humphry-Baker, B. Marsan, S. M. Zakeeruddin and M. Grätzel, *Nat. Chem.*, **2**, 385 (2010).